PHYSICAL REVIEW A **69**, 042322 (2004)

Quantum-state tomography for quadrupole nuclei and its application on a two-qubit system

F. A. Bonk,[1] R. S. Sarthour,[2,*] E. R. deAzevedo,[1,†] J. D. Bulnes,[2] G. L. Mantovani,[1] J. C. C. Freitas,[3] T. J. Bonagamba,[1]
A. P. Guimarães,[2] and I. S. Oliveira[2]
[1]*Instituto de Física de São Carlos, Universidade de São Paulo, P.O. Box 369, São Carlos 13560-970, SP, Brazil*
[2]*Centro Brasileiro de Pesquisas Físicas, Rua Dr. Xavier Sigaud 150, Rio de Janeiro 22290-180, RJ, Brazil*
[3]*Departamento de Física, Universidade Federal do Espírito Santo, Vitória 29060-900, ES, Brazil*
(Received 13 October 2003; revised manuscript received 11 December 2003; published 29 April 2004)

A method for performing quantum state tomography for quadrupole nuclei is presented in this paper. First, it is shown that upon appropriate phase cycling, the nuclear-magnetic-resonance (NMR) intensities of quadrupole nuclei depend only on diagonal elements of the density-matrix. Thus, a method for obtaining the density-matrix elements, which consists of dragging off-diagonal elements into the main diagonal using fine phase-controlled selective radio-frequency pulses, was derived. The use of the method is exemplified through ^{23}Na NMR (nuclear spin $I=3/2$) in a lyotropic liquid crystal at room temperature, in three applications: (a) the tomography of pseudopure states, (b) the tomography of the quadrupole free evolution of the density matrix, and (c) the unitary state evolution of each qubit in the system over the Bloch sphere upon the application of a Hadamard gate. Further applications in the context of pure NMR and in the context of quantum information processing, as well as generalizations for higher spins, are discussed.

DOI: 10.1103/PhysRevA.69.042322 PACS number(s): 03.67.Lx, 33.25.+k, 76.60.−k

I. INTRODUCTION

Nuclear-magnetic-resonance (NMR) quantum computing appeared in the late 1990s as the main candidate for implementation of quantum processors [1]. However, it was soon recognized [2,4] that exponential loss of NMR signal upon increasing number of qubits would pose severe restrictions concerning the scalability of systems for quantum computing in large scale. Such observations stimulated a very interesting debate [5,6] about the capability of NMR to implement true quantum operations, particularly to produce entanglement [1]. In this context, it is rather surprising that not much effort has been directed to the experimental demonstrations of quantum information processing by NMR, in spite of many claims of quantum algorithm implementation [7–9]. For instance, to the best of our knowledge, no experiment has clearly shown the unitarity and reversibility of a one-qubit gate such as the Hadamard gate and its adjoint, or the quantum circuit which generates entanglement [10]. By this we mean experiments where quantum state tomography is implemented at every step of the gate and the trajectory of the one qubit state is traced over the Bloch sphere (see however Ref. [8], where quantum state tomography is implemented for the whole cycle of Grover algorithm).

In this sense, it appears that, from the point of view of pure quantum information processing by NMR, there is still something left to be learnt from one- and two-qubit systems. For this purpose, quadrupole nuclei are particularly well adapted. Implementation of pseudopure states [11], elementary logic gates [12], simulation of quantum systems [13], and relaxation studies [14] have been reported in the recent literature of NMR quantum computing. All these studies were based only on NMR spectral analysis that is, none of them exhibited quantum-state tomography. From the strict point of view of quantum information processing, they are intrinsically less informative, since different density matrices can give rise to the same NMR spectrum. In this paper we report a method for quantum state tomography in quadrupole nuclei. We show that, upon appropriate phase cycling of the selective radio-frequency reading pulses, the NMR intensities will be related only to the density-matrix diagonal elements. After "dragging" the nondiagonal elements to the main diagonal, using phase controlled selective pulses a set of coupled equations was obtained, from which the real and imaginary parts of the density matrix can be determined. We apply the method to a spin $I=3/2$ (two-qubit) system formed by ^{23}Na nuclei in a lyotropic liquid crystal at room temperature. Three applications are shown: (a) the four pseudopure states; (b) the free evolution of the density matrix under quadrupole interaction, and (c) the unitary evolution of a single qubit under the application of a double Hadamard gate. From this experiment, we rebuilt the evolution of the Bloch vector of one qubit over the Bloch sphere.

This paper is organized as follows. The experimental details are given in Sec. II. Some features of the quadrupole systems are presented in Sec. III, and the process for obtaining the quantum state tomography for quadrupole nuclei is discussed in Sec. IV. Finally, the results are presented in Sec. V, followed by the conclusions. The Appendix shows some results of tomographed density matrices compared to calculated ones using ideal rotations.

II. EXPERIMENTAL PROCEDURES

The ^{23}Na NMR experiments described in this paper were performed using a 9.4 T VARIAN INOVA spectrometer in a lyotropic liquid-crystal system prepared with 35.9 wt. % of sodium decyl sulfate (Fluka), 7.2 wt. % of decanol (Su-

---

[*]Email address: sarthour@cbpf.br
[†]Email address: azevedo@if.sc.usp.br

pelco), and 56.9 wt. % deuterium oxide (D_2O, Merck), following the procedure described elsewhere [15]. ^{23}Na NMR data were recorded at room temperature using a home-built single-resonance probe with radio-frequency (rf) Helmholtz-like rectangular coils (only one loop 2.5 cm high and 1 cm wide) separated by 7.5 mm. The geometry of the coils was chosen in order to improve rf magnetic field homogeneity along the sample, which was packed in a 5 mm NMR tube 0.5 cm high. Numerical simulations showed that the rf field homogeneity is higher than 95% over the sample volume. The B_0 field homogeneity was about 0.1 ppm. Gaussian shaped rf pulses were used to perform selective saturation ($\pi/2$) and inversion (π) of populations. Pulse durations were set to provide a multiple of 2π rotations under the quadrupolar interaction in order to minimize possible effects of the quadrupolar evolution during the pulses [20]. The mean rf amplitudes and the frequency offsets were carefully adjusted to satisfy the selectivity condition [16–18]. The experimental calibration was checked against numerical simulations using the full Hamiltonian, which showed that the single-quantum transition, the case of the Hadamard operation on the first qubit, is not affected by the quadrupolar interaction. A nonselective hard $\pi/20$ pulse 1.5 μs long was applied in order to measure the differences of populations for the three pairs of neighbor levels. Experiments were performed with a recycle delay of 500 ms. The ^{23}Na NMR spectra were obtained averaging the free induction decay (FID) signal, obtained for each phase (x, y, $-x$, and $-y$) of the reading $\pi/20$ hard pulse accompanied by the corresponding receiver cycling (standard CYCLOPS scheme). Finally, all the spectra were normalized using the intensities of the equilibrium state.

III. NMR QUADRUPOLE SYSTEMS

The most relevant interactions of a quadrupole nucleus are the Zeeman interaction with a magnetic field and the electric quadrupole moment with an electric field gradient. The Hamiltonian for this system can be described in first order by Eq. (1), where ω_L is the Larmor frequency of the nuclear magnetic moment in the presence of a magnetic field, and ω_Q is the effective quadrupole frequency characterized by the interaction between the nuclear quadrupole moment with the electric-field gradient [19].

$$\mathcal{H} = -\hbar\omega_L \boldsymbol{I}_z + \hbar\omega_Q(3\boldsymbol{I}_z^2 - \boldsymbol{I}^2). \tag{1}$$

For a spin-3/2 system this Hamiltonian gives rise to four unequally spaced energy levels, originating an NMR spectrum containing three lines, corresponding to transitions between adjacent levels (see Fig. 1). These energy states $|3/2\rangle$, $|1/2\rangle$, $|-1/2\rangle$, and $|-3/2\rangle$ can be labeled as $|00\rangle$, $|01\rangle$, $|10\rangle$, and $|11\rangle$ in analogy to two-qubit system containing two $I=1/2$ coupled spins [11,12,14]. From the Hamiltonian, the density matrix can be obtained according to Eq. (2), in the high-temperature regime, where Z is the partition function, n is the number of qubits, and $\beta=1/k_BT$ and $\varepsilon=\beta/2^n \approx 10^{-5}$ for $n=2$ at room temperature.

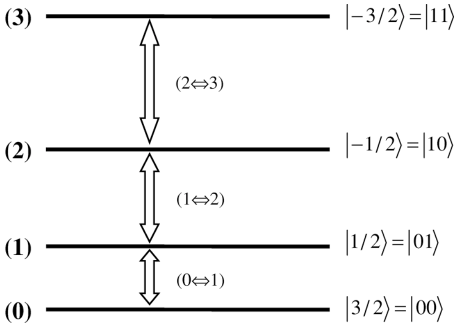

FIG. 1. Schematic representation of the energy levels, for a spin-3/2 system, with their respective labels.

$$\rho = \frac{e^{-\beta\mathcal{H}}}{Z} \approx \frac{1}{2^n}(\boldsymbol{1} - \beta\mathcal{H}) = \frac{\boldsymbol{1}}{2^n} - \varepsilon\mathcal{H}. \tag{2}$$

Since radio-frequency pulses are unitary operations, they act only on the part εH of Eq. (2). Therefore, the measured quantity in NMR experiments is the traceless deviation density matrix, which in the equilibrium is given by

$$\Delta\rho_{eq} = -\varepsilon\mathcal{H}. \tag{3}$$

Before performing quantum computing, it is necessary to prepare the system in a pseudopure state. This can be done using the pulse sequences described by Fung [11] and Sinha [12], and then applying a magnetic field gradient to the system, in order to get rid of undesired off-diagonal elements. In this work, the pseudo-pure states were prepared using the same pulse sequences described in references [11,12], but employing an additional twofold phase cycling (x,y) in the $\pi/2$ pulses as an alternative to the use of magnetic field gradient. The quantum operations were applied to the states obtained for each phase of the $\pi/2$ pulse, which creates the pseudopure states. Therefore, four distinct NMR signals were detected, and the final result, obtained after averaging, was the same as if the quantum gates had been applied to a pseudo pure state. For instance, the sequences for creating the pseudopure state, represented by $\rho_{00}=(1/2^n)(1-\varepsilon)+\varepsilon|00\rangle\langle 00|$, are shown in Eq. (4), where $Y_{\alpha\beta}$ represents a selective $\pi/2$ pulse applied to the transition $(\alpha\Leftrightarrow\beta)$ along y direction, and $\overline{X}_{\alpha\beta}$ represents a selective $\pi/2$ pulse applied to the transition $(\alpha\Leftrightarrow\beta)$ along $-x$ direction. The squared symbols represent selective π pulses:

$$\begin{aligned} U_1 &= X_{23}\cdot Y_{12}^2, \\ U_2 &= \overline{X}_{23}\cdot Y_{12}^2, \\ U_3 &= Y_{23}\cdot Y_{12}^2, \\ U_4 &= \overline{Y}_{23}\cdot Y_{12}^2. \end{aligned} \tag{4}$$

Therefore, the pseudopure state ρ_{00} can be constructed from the equilibrium state ρ_{eq}, as described in Eq. (5).

$$\rho_{00} = \frac{1}{4}\sum_j U_j \rho_{eq} U_j^\dagger . \qquad (5)$$

IV. TOMOGRAPHY METHOD

The density matrix of a general system and, consequently, its deviation contains complex elements, except in the main diagonal, which contains only positive real numbers. In addition, the elements above the main diagonal are the complex conjugate of the ones below, so for a spin-3/2 system deviation density matrices have the general form

$$\Delta\rho = \begin{bmatrix} a & x_a + iy_a & x_b + iy_b & x_c + iy_c \\ x_a - iy_a & b & x_d + iy_d & x_e + iy_e \\ x_b - iy_b & x_d - iy_d & c & x_f + iy_f \\ x_c - iy_c & x_e - iy_e & x_f - iy_f & d \end{bmatrix}. \qquad (6)$$

Therefore, to obtain the quantum-state tomography of any state, it is necessary to determine 16 variables, which are the four real elements of the main diagonal, and the other 12 formed by real and imaginary parts of the nondiagonal elements. For quadrupole systems, the averaged NMR spectrum, obtained after applying the CYCLOPS scheme to the $\pi/20$ reading pulse and receiver, depends only on the diagonal elements of $\Delta\rho$. In fact, for the spin 3/2 system described by $\Delta\rho$, the intensities of each peak of the NMR spectrum obtained after applying the reading scheme are given by Eq. (7).

$$A_1 = \sqrt{3}(e_{11}e_{12}a - e_{12}e_{22}b - e_{23}e_{13}c - e_{13}e_{14}d),$$

$$A_2 = 2(e_{13}e_{12}a + e_{22}e_{23}b - e_{23}e_{22}c - e_{13}e_{12}d),$$

$$A_3 = \sqrt{3}(e_{13}e_{14}a + e_{13}e_{23}b + e_{12}e_{22}c - e_{11}e_{12}d). \qquad (7)$$

The e_{ij} are absolute values of the $\pi/20$ reading pulse matrix elements along any direction, as described in the Appendix. A_1, A_2, and A_3 stand for the NMR spectra intensities for the transitions $(0 \Leftrightarrow 1)$, $(1 \Leftrightarrow 2)$ and $(2 \Leftrightarrow 3)$, respectively. Because observable NMR deviation matrices are traceless, $a+b+c+d=0$, a fourth equation can be added to the system. Therefore, the four diagonal elements can be obtained after measuring each of the line intensities of the averaged spectrum and solving the set of Eq. (7). The first step of the state tomography is to obtain the deviation density matrix main diagonal, by using the process described above. For a spin-3/2 system, the result gives the four diagonal elements, a, b, c, and d of Eq. (6). In order to get the off-diagonal elements and determine the state tomography, rf transition-selective pulses were used. The evolution operators for these pulses can be constructed according to Eq. (8) in the rotating frame.

$$U = \exp(-i \cdot [\mathcal{H} + \hbar\omega_{RF}\boldsymbol{I}_z - \hbar\omega_1 \boldsymbol{I}_\alpha] \cdot t_p/\hbar). \qquad (8)$$

The parameter ω_{RF} is the selective pulse carrier frequency, ω_1 is the amplitude of the rf pulse $(\omega_1 = \gamma B_1)$, $\boldsymbol{I}_\alpha$ is the angular momentum spin operator in the α direction, and t_p is the pulse duration. The effect of the pulse operator is to induce rotations in the spin system, allowing the manipulation of the phase of the off-diagonal elements of the density matrix, and consequently controlling the phase of the quantum state.

A complete set of these ideal pulse matrices is shown in the Appendix. The symbols X_{01} and Y_{23} stand for $\pi/2$ pulses applied to the transition $(0 \Leftrightarrow 1)$ along the x direction and to the transition $(2 \Leftrightarrow 3)$ along the y direction, respectively. The effect of the application of such pulses to the system is to bring the off-diagonal elements of the density matrix to the main diagonal, as it is shown in Eq. (9), where only the main diagonal elements are displayed for simplicity. The experimental procedure for calibration of the pulses is given in Sec. II, and the effects of nonperfect selectivity are discussed in the concluding section.

$$\rho(X_{01}) = X_{01} \cdot \Delta\rho \cdot X_{01}^\dagger = \frac{1}{2}\begin{bmatrix} a + 2y_a + b & & & \\ & a - 2y_a + b & & \\ & & 2c & \\ & & & 2d \end{bmatrix},$$

$$\rho(Y_{23}) = Y_{23} \cdot \Delta\rho \cdot Y_{23}^\dagger = \frac{1}{2}\begin{bmatrix} 2a & & & \\ & 2b & & \\ & & c + 2x_f + d & \\ & & & c - 2x_f + d \end{bmatrix}. \qquad (9)$$

As can be seen from Eq. (9), y_a and x_f are easily determined if the diagonal elements are known. Since the diagonal elements of the density matrix can be obtained by the method described earlier, the real and imaginary parts of the off-diagonal elements are easily obtained. A complete set of equations that allow the determination of all off-diagonal elements of the deviation density matrix is shown in Eq. (10).

$$y_a = [\rho_{11}(X_{01}) - \rho_{22}(X_{01})]/2,$$

$$y_d = [\rho_{22}(X_{12}) - \rho_{33}(X_{12})]/2,$$

$$y_f = [\rho_{33}(X_{23}) - \rho_{44}(X_{23})]/2,$$

$$x_a = [\rho_{11}(Y_{01}) - \rho_{22}(Y_{01})]/2,$$

$$x_d = [\rho_{22}(Y_{12}) - \rho_{33}(Y_{12})]/2,$$

$$x_f = [\rho_{33}(Y_{23}) - \rho_{44}(Y_{23})]/2,$$

$$x_b = [\rho_{22}(X_{12}X_{01}) - \rho_{33}(X_{12}X_{01}) - \sqrt{2}y_d]/\sqrt{2},$$

$$y_b = [\rho_{33}(Y_{12}X_{01}) - \rho_{22}(Y_{12}X_{01}) + \sqrt{2}x_d]/\sqrt{2},$$

$$x_e = [\rho_{33}(X_{23}X_{12}) - \rho_{44}(X_{23}X_{12}) - \sqrt{2}y_f]/\sqrt{2},$$

$$y_e = [\rho_{44}(Y_{23}X_{12}) - \rho_{33}(Y_{23}X_{12}) + \sqrt{2}x_f]/\sqrt{2},$$

$$x_c = \rho_{33}(Y_{23}Y_{12}Y_{01}) - \rho_{44}(Y_{23}Y_{12}Y_{01}) - \sqrt{2}x_f + x_e,$$

$$y_c = \rho_{44}(X_{23}X_{12}X_{01}) - \rho_{33}(X_{23}X_{12}X_{01}) + \sqrt{2}y_f + x_e. \quad (10)$$

The expression $\rho_{kk}(X_{mn}, \ldots, Y_{ij})$ stands for the diagonal element (kth line and kth column) of the deviation density matrix after the application of the respective $(X_{mn}, \ldots, Y_{ij})$ pulse sequence, from right to left. Because the main diagonal was obtained beforehand, the whole matrix is known. In summary, the method to obtain the deviation density matrix—*state tomography*—consists of determining its diagonal elements, after performing operations on the system, which drag the off-diagonal elements into the main diagonal. Double-quantum selective pulses can also be used for determining the elements ρ_{13}, ρ_{24}, and ρ_{14}, and this method has the advantage of utilizing a smaller number of pulses, as it is shown in Eq. (11). However, all the results described in this paper were obtained using single-quantum selective pulses.

$$x_b = [\rho_{11}(Y_{02}) - \rho_{33}(Y_{02})]/2,$$

$$y_b = [\rho_{11}(X_{02}) - \rho_{33}(X_{02})]/2,$$

$$x_e = [\rho_{22}(Y_{13}) - \rho_{44}(Y_{13})]/2,$$

$$y_e = [\rho_{22}(X_{13}) - \rho_{44}(X_{13})]/2,$$

$$x_c = [\rho_{44}(Y_{23}Y_{13}) - \rho_{33}(Y_{23}Y_{13}) + \sqrt{2}x_f]/\sqrt{2},$$

$$y_c = [\rho_{44}(Y_{23}X_{13}) - \rho_{33}(Y_{23}X_{13}) + \sqrt{2}x_f]/\sqrt{2}. \quad (11)$$

It is also possible to use multifrequency pulses, so that many imaginary (or real) parts of different elements can be obtained simultaneously. As an example, for spin 3/2, one can excite the transitions $(0 \Leftrightarrow 1)$ and $(2 \Leftrightarrow 3)$ using a single two-frequency pulse. Since these pulses operate on completely different quantum states, parts of the elements ρ_{12} and ρ_{34} can be obtained from the new diagonal elements, simultaneously [see Eq. (9)]. The use of multifrequency pulses becomes more interesting for higher spin systems. The operators of the selective pulses are easily obtained for other quadrupole systems with higher values of spin, and they have the same form of Eq. (8). In addition, the equations for each matrix element are easily found by applying the ideal pulse operators pulses on $\Delta\rho$. As a result, the quantum state tomography process described here can be straightforwardly extended to any quadrupole system, provided that the NMR spectrometer allows the application of selective pulses with reliable phase control.

V. EXPERIMENTAL RESULTS

The procedure of quantum state tomography described in this paper was applied to a spin-3/2 system, using single-quantum selective pulses. The deviation density matrix was obtained experimentally for several coherent states. The tomography of the equilibrium state was also found, and is presented in Fig. 2. The real and imaginary parts of the measured matrix are shown on the left and right hand side of figure, respectively. The simulated and experimentally determined deviation density matrices for this state are described in the Appendix.

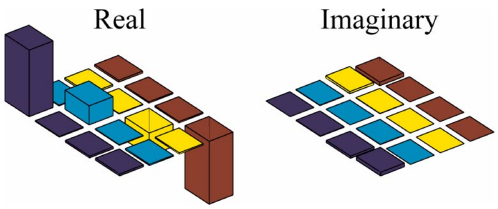

FIG. 2. (Color online) Quantum state tomography the deviation matrix of the equilibrium state of ^{23}Na ($I=3/2$, two qubits). The real and imaginary parts of the density matrix are shown on the left and right hand side, respectively.

A. Pseudopure states

The tomography of the deviation density matrices representing the four pseudopure states, which we will label $\Delta\rho_{00}$, $\Delta\rho_{01}$, $\Delta\rho_{10}$, and $\Delta\rho_{11}$ were obtained, and they are presented in Fig. 3, where only the real part is shown for simplicity, since the contribution of the imaginary part is irrelevant to these states (see the numerical results in the Appendix). The simulated and experimentally determined deviation density matrices for each one of the pseudopure states are also described in the Appendix.

B. Unitary Hadamard evolution

The Hadamard gate is an one-qubit quantum gate, and for quadrupole systems it can be constructed using two selective pulses, as reported in Ref. [14] Both pulses have the same frequency—the same as the first transition $(0 \Leftrightarrow 1)$; however, the first one is a $\pi/2$ pulse applied along the y direction, and the last one is a π pulse along the $-x$ direction. The evolution of this gate was followed, for each individual stage—after the application of each selective pulse—when it was applied twice to the initial pseudopure state ρ_{00}. The real part of the state tomography for the four stages (one for each pulse) of

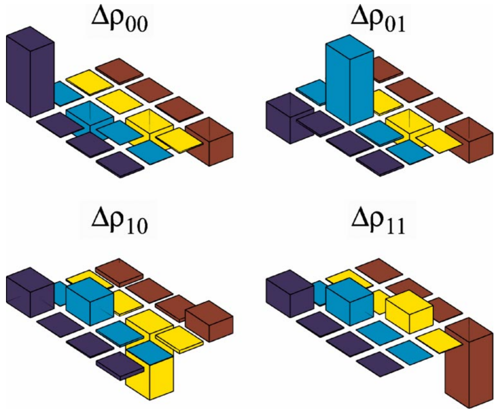

FIG. 3. (Color online) The real part of the quantum-state tomography for the deviation matrices representing the four pseudopure states, as described in the text.

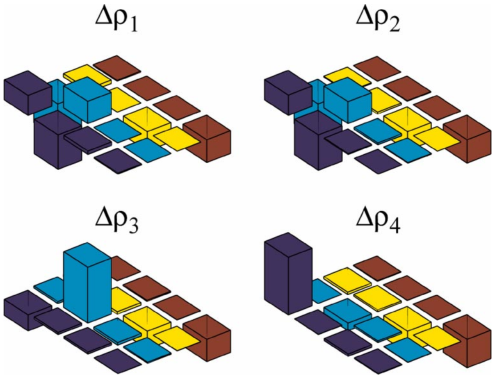

FIG. 4. (Color online) The real part of the quantum tomography after each stage of the Hadamard, as explained in the text.

the H^2 (Hadamard gate applied twice) sequence are presented in Fig. 4, where the symbols in the figure stand for: $\Delta\rho_1$ (after Y_{01}), $\Delta\rho_2$ (after $\overline{X}_{01}^2 \cdot Y_{01}$), $\Delta\rho_3$ (after $Y_{01} \cdot \overline{X}_{01}^2 \cdot Y_{01}$), and $\Delta\rho_4$ (after $\overline{X}_{01}^2 \cdot Y_{01} \cdot \overline{X}_{01}^2 \cdot Y_{01}$). At the first stage of the process the populations of the first two levels, $|00\rangle$ and $|01\rangle$, are equally splitted between the two lower levels. At the second stage, the relative phases are manipulated. The system is then taken to the pseudopure state ρ_{01} at the third stage. The initial state is recovered at the fourth and final stage. An important imaginary contribution was detected after the first stage of the Hadamard gate, which does not appear in the simulations with ideal pulses. This shows that the action of the experimental selective pulse applied to the system deviates from the ideal (theoretical), which is due to several factors and will be discussed in the conclusions. Nevertheless, this imaginary part disappears at the end of the whole process, and the self-reversibility of the Hadamard gate is demonstrated. The simulated, and experimentally determined density matrix for the four stages of the Hadamard gate, are also presented in the Appendix.

As it can be seen in the Appendix, the experimental results have a fairly good agreement with the simulated ones. The small difference observed before and after the application of the double Hadamard gate is due a number of different causes, one of which is the transverse relaxation. The application of Hadamard gate takes about 2 ms ($\sim$500 μs for each pulse), and the preparation of the pseudopure state takes about 1 ms. Therefore, the full operation of the Hadamard gate takes $\sim$3 ms, which is of the order of T_2 in this system. We investigated the effects of other contributions performing numerical simulations, which included the relaxation effects, B_0 and rf field inhomogeneity, errors in the pseudopure state preparation, deviation from perfect rf pulse selectivity, and, finally, phase deviation, which includes rf phases and phase errors in the states. These simulations indicated that all these effects contribute to the error in the phase of the final state, as observed in Fig. 6. As can be observed in Fig. 4, the Hadamard gate is acting only on the qubit $b(|ab\rangle)$, while the qubit a remains practically unchanged during this operation.

C. Quadrupolar free evolution

As a third example of quantum-state tomography application, the free evolution of the density matrix was studied after the application of a single $\pi/2$ hard pulse, where the carrier frequency was set on the transition $(1 \Leftrightarrow 2)$. The result is shown in Fig. 5, where the points are experimental data and dashed lines are computer simulations for this particular quadrupole system. As can be seen from Fig. 5, the components of the elements $\rho_a(\rho_a = x_a + iy_a)$ and ρ_f oscillate with the quadrupolar frequency, while ρ_d remains unchanged, because, contrarily to the transitions $(0 \Leftrightarrow 1)$ and $(2 \Leftrightarrow 3)$, in

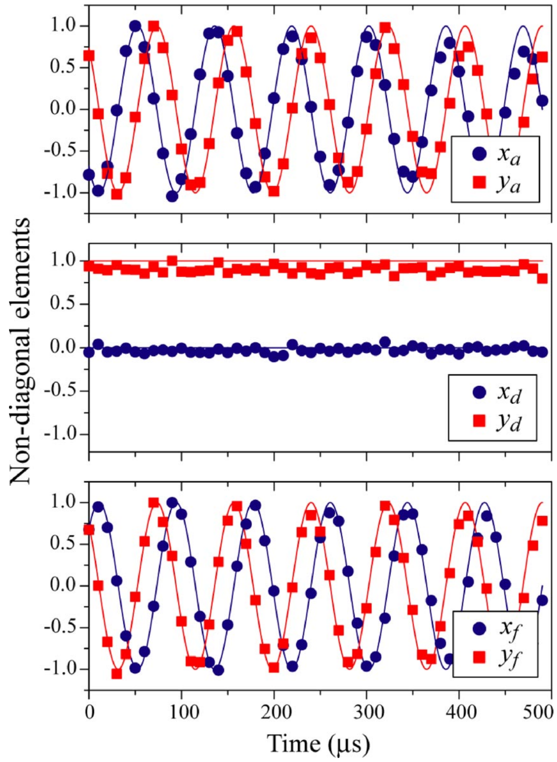

FIG. 5. (Color online) Free evolution of the x_a, y_a, x_d, y_d, x_f, and y_f elements, after a hard $\pi/2$ pulse. The points are experimental results while the lines are numerical simulations of the system.

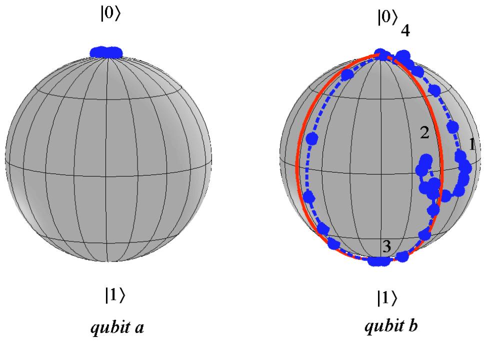

FIG. 6. (Color online) The trajectory of the Bloch vector, for each individual qubit, during the Hadamard gate evolution. The points are experimental results, the dotted blue line is an interpolation of the experimental data and the continuous red line is a numerical simulation. Numbers indicate the end of each step (rf pulse), and the points between the numbers correspond to matrices tomographed from the application of the selective rf pulses in several steps along their Gaussian envelopes (intermediate angles), acquired for completeness.

first order the transition $(1 \Leftrightarrow 2)$ does not depend on the quadrupole interaction.

VI. DISCUSSION AND CONCLUSIONS

The evolution of an one-qubit state represented by a density matrix ρ can be visualized through the motion of its Bloch vector over the Bloch sphere. The density matrix for the individual qubits can be obtained from the partial trace [10] of the full density matrix of the system, which in this case involves two qubits. In order to do so, (1/4)th of a unity matrix was added to $\varepsilon\Delta\rho(\varepsilon \approx \mu H_0/k_B T \approx 10^{-5})$, where $\Delta\rho$ is the tomographed deviation density matrix for each individual qubit, the Bloch vector for each one of them was obtained according to Eq. (12) [10].

$$\rho(t) = \frac{1 + \boldsymbol{r}(t) \cdot \sigma}{2}. \tag{12}$$

The symbol σ represents a vector whose components are the Pauli's matrices, and $\boldsymbol{r}(t)$stands for the unit Bloch vector, at a time t, which can be followed even during a logical operation, for each qubit. As a result, the trajectory on the Bloch sphere was determined, during the application of a double Hadamard gate on the qubit $b(|ab\rangle)$ as presented in Fig. 6, where the points were obtained from Eq. (12). The (red) continuous line is a numerical simulation, using ideal pulses (see the Appendix), and the dotted blue line is an interpolation of the experimental points. As it can be seen from the figure, the qubit b evolves according to the theoretical predictions, while the qubit a remains basically unchanged during the whole process.

After the application of the first pulse of the Hadamard gate ($\pi/2$ around y, number 1 in Fig. 6), one can notice that the state of qubit b does not evolve as predicted by the simulations using the ideal pulses and the state after the first pulse of the Hadamard gate is off the x axis (the possible causes for this effect are discussed below). Therefore, when the second pulse of the Hadamard gate is applied, the qubit b undergoes a rotation of π around the x direction, as clearly seen in the semicircle from number 1 to number 2 in Fig. 6. The initial and final one-qubit states are very close, which demonstrates the self-reversibility of the Hadamard gate.

In the quantum tomography procedure proposed in this paper, we neglected a number of effects, which—added together—contribute to the errors in the tomographed deviation density matrix and to the difference between the ideal trajectory and the experimental data observed in Fig. 6 (a relative error of about $\sim 15°/360° = 4\%$). The possible sources of errors are (1) nonperfect selective pulses, (2) relaxation effects, (3) B_0 and B_1 field inhomogeneities, and (4) relative phase errors associated to rf pulses applied along $\pm x$ and $\pm y$ axes in the rotating frame. Most of them can be minimized through a good calibration of the selective rf pulses and the use of high homogeneity for B_0 and B_1 magnetic fields (as described in the experimental section). However, residual imperfections will always remain. Because the tomography method has to distinguish the imaginary from the real components of each element of the deviation density matrix, phase errors are expected to be more important in the case of superposition states like the Hadamard gate. Such errors were numerically estimated by introducing spurious phase contributions in the ideal pulse matrix, and simulating the tomography process. The full Hamiltonian was also considered in these simulations, allowing an estimate of the error introduced by the use of ideal rotations. The results are as follows.

First, we consider the selectivity. Because in our experiments was ω_1/ω_Q chosen to be approximately 0.02, the error due to nonperfect selectivity is less than 1% per applied pulse. This small effect is apparent in Fig. 6 as a slight change for the Bloch vector associated to qubit a. Another important source of error is the spin-spin relaxation (spin-lattice relaxation time is too long, compared to the time scale of the experiment [14]), which combined with the nonselectivity produces a phase error of at most 2° per applied pulse. Also, small uncertainties in the quadrature of the spectrometer (maximum of 2°, for the equipment used) and B_1 field inhomogeneity can produce a total phase deviation of at most 4° per applied pulse. Added together, these sources account for a total phase deviation per applied pulse of at most 5°. Assuming this phase error per pulse, it is possible to estimate the intrinsic uncertainty involved in the tomographed data introducing them into the matrices that represent the pulses in the simulation. With this, we arrived to a percent error of at most 6% (for the main diagonal) upto 9% (for high-order coherences). It should be noted that this error tends to increase for higher-order coherences. This is confirmed by the good agreement between the experimental and simulated density matrices, for the equilibrium and pseudostates, where fewer pulses with proper phase cycling were used. However, these errors accumulate during the execution of a quantum gate such as the Hadamard gate, producing states deviations, such as observed in Fig. 6.

In summary, the quantum-state tomography has been successfully implemented for the first time (to the best of authors' knowledge) for a quadrupole system. The experimental results are in good agreement with the calculated ones, and this process can be easily extended for higher spin values. The quantum-state tomography of the Hadamard evolution and the trajectory of the Bloch vector on the Bloch sphere demonstrate that one and two qubits logical operations can be implemented on quadrupole systems.

ACKNOWLEDGMENTS

The authors acknowledge support from CAPES, CNPq, and FAPESP. R.S.S. especially acknowledges the Brazilian Quantum Information—CNPq project—and the CAPES Prodoc grant program. A special thanks to E. L. G. Vidoto for constructing the NMR probe.

APPENDIX

Ideal selective pulses are used to derive the equations that determine the nondiagonal density matrix elements.

$$X_{01}=\begin{bmatrix}\frac{1}{\sqrt{2}} & \frac{i}{\sqrt{2}} & 0 & 0\\ \frac{i}{\sqrt{2}} & \frac{1}{\sqrt{2}} & 0 & 0\\ 0 & 0 & 1 & 0\\ 0 & 0 & 0 & 1\end{bmatrix},\quad Y_{01}=\begin{bmatrix}\frac{1}{\sqrt{2}} & \frac{1}{\sqrt{2}} & 0 & 0\\ \frac{-1}{\sqrt{2}} & \frac{1}{\sqrt{2}} & 0 & 0\\ 0 & 0 & 1 & 0\\ 0 & 0 & 0 & 1\end{bmatrix},$$

$$X_{12}=\begin{bmatrix}1 & 0 & 0 & 0\\ 0 & \frac{1}{\sqrt{2}} & \frac{i}{\sqrt{2}} & 0\\ 0 & \frac{i}{\sqrt{2}} & \frac{1}{\sqrt{2}} & 0\\ 0 & 0 & 0 & 1\end{bmatrix},\quad Y_{12}=\begin{bmatrix}1 & 0 & 0 & 0\\ 0 & \frac{1}{\sqrt{2}} & \frac{1}{\sqrt{2}} & 0\\ 0 & \frac{-1}{\sqrt{2}} & \frac{1}{\sqrt{2}} & 0\\ 0 & 0 & 0 & 1\end{bmatrix},$$

$$X_{23}=\begin{bmatrix}1 & 0 & 0 & 0\\ 0 & 1 & 0 & 0\\ 0 & 0 & \frac{1}{\sqrt{2}} & \frac{i}{\sqrt{2}}\\ 0 & 0 & \frac{i}{\sqrt{2}} & \frac{1}{\sqrt{2}}\end{bmatrix},\quad Y_{23}=\begin{bmatrix}1 & 0 & 0 & 0\\ 0 & 1 & 0 & 0\\ 0 & 0 & \frac{1}{\sqrt{2}} & \frac{1}{\sqrt{2}}\\ 0 & 0 & \frac{-1}{\sqrt{2}} & \frac{1}{\sqrt{2}}\end{bmatrix}.$$

The e_{ij} coefficients are the absolute values of the $\pi/20$ hard reading pulse.

$$e_{ij}=\begin{bmatrix}0.9908 & 0.1351 & 0.0106 & 0.0005\\ 0.1351 & 0.9785 & 0.1555 & 0.0106\\ 0.0106 & 0.1555 & 0.9785 & 0.1351\\ 0.0005 & 0.0106 & 0.1351 & 0.9908\end{bmatrix}.$$

Experimental results are compared with simulated ones, for the equilibrium state and the pseudopure ones.

$$\Delta\rho_{eq}^{sim}=\frac{1}{2}\begin{bmatrix}3 & 0 & 0 & 0\\ 0 & 1 & 0 & 0\\ 0 & 0 & -1 & 0\\ 0 & 0 & 0 & -3\end{bmatrix},$$

$$\Delta\rho_{00}^{sim}=\frac{1}{2}\begin{bmatrix}3 & 0 & 0 & 0\\ 0 & -1 & 0 & 0\\ 0 & 0 & -1 & 0\\ 0 & 0 & 0 & -1\end{bmatrix},$$

$$\Delta\rho_{01}^{sim}=\frac{1}{2}\begin{bmatrix}-1 & 0 & 0 & 0\\ 0 & 3 & 0 & 0\\ 0 & 0 & -1 & 0\\ 0 & 0 & 0 & -1\end{bmatrix},$$

$$\Delta\rho_{10}^{sim}=\frac{1}{2}\begin{bmatrix}1 & 0 & 0 & 0\\ 0 & 1 & 0 & 0\\ 0 & 0 & -3 & 0\\ 0 & 0 & 0 & 1\end{bmatrix},$$

$$\Delta\rho_{11}^{sim}=\frac{1}{2}\begin{bmatrix}1 & 0 & 0 & 0\\ 0 & 1 & 0 & 0\\ 0 & 0 & 1 & 0\\ 0 & 0 & 0 & -3\end{bmatrix},$$

$$\Delta\rho_{eq}^{\exp}=\begin{bmatrix}1.50 & -0.02-0.01i & -0.04+0.05i & 0.04-0.08i\\ -0.02+0.01i & 0.43 & -0.01-0.01i & -0.03\\ -0.04-0.05i & -0.01+0.01i & -0.51 & -0.03\\ 0.04+0.08i & -0.03 & -0.03 & -1.42\end{bmatrix},$$

$$\Delta\rho_{00}^{\exp}=\begin{bmatrix}1.50 & -0.01-0.01i & 0.03-0.02i & -0.04+0.02i\\ -0.01+0.01i & -0.44 & 0 & -0.01i\\ 0.03+0.02i & 0 & -0.51 & 0.03+0.02i\\ -0.04-0.02i & 0.01i & 0.03-0.02i & -0.55\end{bmatrix},$$

$$\Delta\rho_{01}^{\exp}=\begin{bmatrix}-0.60 & 0.04+0.03i & 0.03-0.02i & 0.04-0.03i\\ 0.04-0.03i & 1.50 & -0.04-0.04i & 0.01\\ 0.03+0.02i & -0.04+0.04i & -0.42 & -0.01i\\ 0.04+0.03i & 0.01 & 0.01i & -0.48\end{bmatrix},$$

$$\Delta\rho_{10}^{\exp} = \begin{bmatrix} 0.58 & 0.01 & -0.03+0.02i & -0.09-0.12i \\ 0.01 & 0.54 & -0.04-0.04i & -0.01+0.06i \\ -0.03-0.02i & -0.04+0.04i & -1.50 & 0.07-0.01i \\ -0.09+0.12i & -0.01-0.06i & 0.07+0.01i & 0.38 \end{bmatrix},$$

$$\Delta\rho_{11}^{\exp} = \begin{bmatrix} 0.52 & 0.02+0.03i & 0.01-0.01i & -0.01-0.01i \\ 0.02-0.03i & 0.53 & 0 & 0 \\ 0.01+0.01i & 0 & 0.44 & 0.01+0.01i \\ -0.01+0.01i & 0 & 0.01-0.01i & -1.50 \end{bmatrix}.$$

Experimental results are compared with simulated ones, for the four stages of the Hadamard sequence.

$$\Delta\rho_{1}^{sim} = \frac{1}{2}\begin{bmatrix} 1 & -2 & 0 & 0 \\ -2 & 1 & 0 & 0 \\ 0 & 0 & -1 & 0 \\ 0 & 0 & 0 & -1 \end{bmatrix}, \quad \Delta\rho_{2}^{sim} = \frac{1}{2}\begin{bmatrix} 1 & -2 & 0 & 0 \\ -2 & 1 & 0 & 0 \\ 0 & 0 & -1 & 0 \\ 0 & 0 & 0 & -1 \end{bmatrix},$$

$$\Delta\rho_{3}^{sim} = \frac{1}{2}\begin{bmatrix} -1 & 0 & 0 & 0 \\ 0 & 3 & 0 & 0 \\ 0 & 0 & -1 & 0 \\ 0 & 0 & 0 & -1 \end{bmatrix}, \quad \Delta\rho_{4}^{sim} = \frac{1}{2}\begin{bmatrix} 3 & 0 & 0 & 0 \\ 0 & -1 & 0 & 0 \\ 0 & 0 & -1 & 0 \\ 0 & 0 & 0 & -1 \end{bmatrix}$$

$$\Delta\rho_{1}^{\exp} = \begin{bmatrix} 0.44 & -0.75+0.26i & 0.00+0.00i & 0.02-0.02i \\ -0.75-0.26i & 0.50 & -0.03-0.03i & 0.02-0.02i \\ 0.00-0.00i & -0.03+0.03i & -0.45 & -0.00+0.02i \\ 0.02+0.018i & 0.02+0.02i & -0.01-0.00i & -0.49 \end{bmatrix},$$

$$\Delta\rho_{2}^{\exp} = \begin{bmatrix} 0.64 & -0.87-0.15i & -0.03+0.03i & 0.01-0.01i \\ -0.87+0.15i & 0.5000 & -0.030-0.03i & 0.03+0.00i \\ -0.03-0.03i & -0.03+0.03i & -0.53 & -0.00-0.00i \\ 0.01+0.01i & 0.03-0.00i & -0.00+0.00i & -0.61 \end{bmatrix},$$

$$\Delta\rho_{3}^{\exp} = \begin{bmatrix} -0.23 & -0.03-0.09i & 0.03-0.02i & 0.07-0.03i \\ -0.03+0.09i & 1.5 & -0.07-0.08i & 0.02-0.03i \\ 0.03+0.02i & -0.07+0.08i & -0.59 & -0.03-0.02i \\ 0.07+0.03i & 0.02+0.03i & -0.03+0.02i & -0.68 \end{bmatrix},$$

$$\Delta\rho_{4}^{\exp} = \begin{bmatrix} 1.5 & -0.08+0.21i & -0.06+0.02i & -0.08+0.00i \\ -0.08-0.21i & -0.23 & -0.00-0.01i & -0.01+0.00i \\ -0.06-0.02i & 0.00+0.01i & -0.58 & 0.04+0.03i \\ -0.08-0.00i & -0.01-0.00i & 0.04-0.03i & -0.6934 \end{bmatrix}.$$

---

[1] J. A. Jones, Prog. Nucl. Magn. Reson. Spectrosc. **38**, 325 (2001).

[2] S. L. Braunstein, C. M. Caves, R. Jozsa, N. Linden, S. Popescu, and R. Schack, Phys. Rev. Lett. **83**, 1054 (1999).

[3] N. Linden and S. Popescu, Phys. Rev. Lett. **87**, 047901-1 (2001).

[4] R. Laflamme, D. Cory, C. Negrevergne, and L. Viola, Quantum Inf. Comput. **2**, 166 (2002).

[5] See R. Laflamme, http://quickreviews.org/cgi/display.cgi?reviewID5laf.q-p.9811 018.

[6] G. L. Long, H. Y. Yan, Y. S. Li, C. C. Tu, S. J. Zhu, D. Ruan, Y. Sun, J. X. Tao, and H. M. Chen, Commun. Theor. Phys. **38**, 305 (2002).

[7] M. A. Nielsen, E. Knill, and R. Laflamme, Nature (London) **396**, 52 (1998).

[8] I. L. Chuang, N. Gershenfeld, and M. Kubinec, Phys. Rev. Lett. **80**, 3408 (1998).

[9] L. M. K. Vandersypen, M. Steffen, G. Breyta, C. S. Yannoni, M. H. Sherwood, and I. L. Chuang, Nature (London) **414**, 883 (2001).

[10] M. A. Nielsen and I. Chuang, *Quantum Computation and Quantum Information* (Cambridge University Press, Cambridge, 2002).

[11] A. K. Khitrin and B. M. Fung, J. Chem. Phys. **112**, 6963 (2000).

[12] N. Sinha, T. S. Mahesh, K. V. Ramanathan, and A. Kumar, J. Chem. Phys. **114**, 4415 (2001).

[13] A. K. Khitrin and B. M. Fung, Phys. Rev. A **64**, 032306 (2001).

[14] R. S. Sarthour, E. R. deAzevedo, F. A. Bonk, E. L. G. Vidoto, T. J. Bonagamba, A. P. Guimarães, J. C. C. Freitas, and I. S. Oliveira, Phys. Rev. A **68** 022311 (2003).

[15] K. Radley, L. W. Reeves, and A. S. Tracey, J. Phys. Chem. **80**, 174 (1976).

[16] A. Wokaun and R. R. Ernst, Chem. Phys. Lett. **52**, 407 (1977).

[17] S. Vega and A. Pines, J. Chem. Phys. **66**, 5624 (1977).

[18] S. Vega, J. Chem. Phys. **68**, 5518 (1978).

[19] C. P. Slichter, *Principles of Magnetic Resonance* (Springer-Verlag, Berlin, 1990).

[20] R. Das and A. Kumar, Phys. Rev. A **68**, 032304 (2003).